Mechanistic origins of bombardier beetle (Brachinini) explosion-induced defensive spray pulsation

Citation: Arndt, E. M. et al. "Mechanistic Origins of Bombardier Beetle (Brachinini) Explosion-Induced Defensive Spray Pulsation." Science 348.6234 (2015): 563–567.

As Published: http://dx.doi.org/10.1126/science.1261166

Publisher: American Association for the Advancement of Science (AAAS)

Persistent URL: http://hdl.handle.net/1721.1/96867

Version: Author's final manuscript: final author's manuscript post peer review, without publisher's formatting or copy editing

Title: Mechanistic Origins of Bombardier Beetle (Brachinini) Explosion-Induced Defensive Spray Pulsation

Authors: Eric M. Arndt[1], Wendy Moore[2], Wah-Keat Lee[3], Christine Ortiz[1,*]

Affiliations:

[1]Department of Materials Science and Engineering, Massachusetts Institute of Technology, Cambridge, MA 02139-4307, USA.

[2]Department of Entomology, The University of Arizona, Tucson, AZ 85721-0036, USA.

[3]National Synchrotron Light Source II, Brookhaven National Laboratory, Upton, NY 11973-5000, USA.

*Correspondence to: cortiz@mit.edu

Abstract:

Bombardier beetles (Brachinini) utilize a rapid series of discrete explosions inside their pygidial gland reaction chambers to produce a hot, pulsed, quinone-based defensive spray. The mechanism of brachinines' spray pulsation was explored using anatomical studies and direct observation of explosions inside living beetles using synchrotron X-ray imaging. Quantification of the dynamics of vapor inside the reaction chamber indicates that spray pulsation is controlled by specialized, contiguous cuticular structures located at the junction between the reservoir (reactant) and reaction chambers. Kinematics models suggest passive mediation of spray pulsation by mechanical feedback from the explosion causing displacement of these structures.

One Sentence Summary: Spray pulsation in bombardier beetles was determined to be controlled by the displacement of specialized cuticular structures between the reservoir (reactant) and reaction chambers.

Main Text:

When threatened, bombardier beetles (Fig. 1A) expel a hot spray from their pygidial glands (*1*, *2*). The spray contains *p*-benzoquinones (*3*), chemical irritants commonly employed by arthropods (*4*). However, bombardier beetles are unique in utilizing an internal explosive chemical reaction to simultaneously synthesize, heat, and propel their sprays (*2*, *3*). The spray dynamics have been investigated by high-speed photography of the spray, spray impact force measurements, recordings of explosion sounds, and simulations (*5*-*7*). Species in the tribe Brachinini (brachinines) achieve spray temperatures of ~100 °C (*2*) with ranges of several centimeters (*1*) and velocities of ~10 m/s via a "biological pulse jet" (*5*), where the spray consists of a rapid succession of pulses formed in discrete explosions. Pulse repetition rates of 368-735 Hz were measured from audio recordings for *Stenaptinus insignis* (*5*).

It is well known that brachinines' ability to produce internal explosions is facilitated by the two-chambered construction of their pygidial glands (*3*) (Fig. 1B-E). Each of the beetle's two pygidial glands comprises a reservoir chamber (RSC), reaction chamber (RXC), and exit channel (EC) which vents near the abdomen tip (Fig. 1B). The distal ends of the exit channels curve dorsally to form reflector plates (Fig. 1B, RP) used for spray aiming (*8*). An inter-chamber valve (Fig. 1D,E, ICV) is contiguous with the walls of the reaction and reservoir chambers and separates the chambers' contents when closed (*2*). The pygidial glands are constructed of cuticle,

a composite of chitin, proteins, and waxes (*9*), which protects the beetle from the toxic chemicals, high temperatures, and high pressures during explosions. The muscle-enveloped, flexible reservoir chamber (*5*) stores an aqueous reactant solution of ~25% hydrogen peroxide and ~10% *p*-hydroquinones (*3*), along with ~10% alkanes as a nonreactive second liquid phase (*10*). Valve muscles (Fig. 1D, VM) span between the valve and the reservoir chamber to facilitate valve opening. During spray emission, reactant solution flows from the reservoir chamber into the reaction chamber, where it reacts with a solution of peroxidase and catalase enzymes (*11*) to form *p*-benzoquinones and explosively liberate oxygen gas, water vapor, and heat, propelling a hot, noxious spray out the exit channel.

The mechanism of brachinines' spray pulsation has not been understood because previous studies, relying on external observations, have not probed internal dynamics. Here, we investigate this open question through optical and scanning electron microscopy to obtain new insights into the pygidial gland anatomy and synchrotron X-ray imaging (*12-16*) at up to 2000 frames per second (fps) to directly observe internal dynamics of spray pulsation in live beetles (*Brachinus elongatulus*) (*17*). These experiments provide an understanding of how explosions are initiated inside the pygidial glands and allow identification of the specific gland structures that mediate spray pulsation. An understanding of how brachinine pygidial glands produce (and survive) repetitive explosions could provide new design principles for technologies such as blast mitigation and propulsion.

Optical microscopy reveals that the reaction chamber exhibits dramatic spatial heterogeneity in cuticle sclerotization (Fig. 1C), corresponding to regions with different flexibility/rigidity (*18*) and, presumably, functional significance. The cuticle of most of the reaction chamber is tan or brown, implying heavy sclerotization and therefore high stiffness which would serve to limit wall deflection and protect the beetle's internal tissues from the explosions. However, several regions are colorless (stained blue in Fig. 1B,C to increase contrast) and, hence, lightly sclerotized and compliant. These regions include the reaction chamber's dorsal midline crease and the junction between the reaction chamber and the exit channel (Fig. 1C). Similarly, the dorsal part of the exit channel is membranous and lightly sclerotized whereas the ventral part is thick and heavily sclerotized (Fig. 1C) (*6*). SEM of the inter-chamber region in cross-section (Fig. 1E) reveals that the cuticle which connects the valve to the dorsal part of the reaction chamber (hereafter called the expansion membrane; labeled EM) is very thin (~200 nm) and wrinkled, suggesting high flexibility.

Vapor formation during each explosion is clearly seen in the X-ray video as a bright region within the reaction chamber (Fig. 2A, movie S1). In the first pulse, vapor forms in the reaction chamber and propagates towards the exit channel. With each subsequent pulse, vapor advances slightly within the reaction chamber to occupy greater volume (implied by increased area) and then recedes (Fig. 2A, first five pulses shown). Average pulsation rates calculated for 35 instances of gland activity from 18 sprays (median number of explosions, 13; range, 2-46) ranged from 341-976 Hz (median, 667 Hz; mean ± SD, 698 ± 146 Hz) (figure S1, table S2). A linear fit to active time vs. number pulses predicts a pulsation rate of 650 Hz ($R^2 = 0.88$). These results are consistent with external experimental measurements of *S. insignis* (*5*) and approach the maximum rates reported for cyclic insect motions such as wing beats, measured as high as 1000 Hz for midges (*19*).

Each explosion corresponds to the injection of a reactant droplet into the reaction chamber which can sometimes be seen as a dark circle in relief against bright vapor (Fig. 2B;

movie S2). Maximum diameters measured 208 ± 7 μm (mean ± SD) for four clearly visualized droplets. Assuming sphericity, the droplet volume is calculated to be 4.7 ± 0.5 nL, and the mass is estimated as 5.5 ± 0.6 μg. Based on the theoretical heat of reaction of 0.8 J/mg (*2*), the estimated energy release for each explosion is 4×10^{-3} J, and this energy liberates heat, boils water, and to a lesser extent provides the kinetic energy of the spray pulse. Estimating the spray pulse mass as equivalent to the droplet mass and taking 10 m/s for the spray exit velocity (*5*), the kinetic energy of a spray pulse is calculated to be 3×10^{-7} J. Equating this energy to work done by pressure, the average overpressure in the reaction chamber is estimated as 20 kPa, producing wall tensile stresses of ~1 MPa. For comparison, cuticle tensile strengths are typically tens to hundreds of megapascals (*20*). The time required to expel a pulse is estimated as 0.1 ms from the spray velocity and gland dimensions, consistent with the fact that explosions typically occur within single 2000-fps video frames (0.5 ms).

During each explosion, vapor is observed to fill a convex region between the reservoir and reaction chambers (Fig. 2A) that exceeds the dimensions of the reaction chamber indicated by microscopy (figure S2), suggesting outwards displacement of the expansion membrane driven by the explosion overpressure. Using the convex vapor shape as a proxy, the stretched expansion membrane can be modeled as a hemi-ellipsoid (figure S2) and its maximum extension is found to be approximately 280% (supplementary online text). For comparison, some insect cuticles exhibit recoverable extensions of 1000% (*21*). Based on the estimated overpressure and the estimated mass of the hemolymph displaced as the expansion membrane displaces into the body cavity, the expansion occurs with a maximum velocity of 6 m/s, attaining maximum displacement in 0.06 ms (supplementary online text), consistent with the observation that expansion occurs within one video frame (0.5 ms). About one video frame after expansion is observed, the explosion reaction stops and vapor in the inter-chamber region contracts (e.g. Fig. 2A frame 16), implying that the expansion membrane has returned to its unexpanded shape.

The exit channel of an active gland remains vapor-filled, and therefore open, throughout the entire pulse cycle (Fig. 2A, movies S1-S3), possibly due to shape or mechanical characteristics (e.g. viscoelasticity) of its dorsal membrane, indicating that control of spray pulsation is accomplished by the reaction chamber inlet structures alone through opening and closing of the inter-chamber valve, as hypothesized previously (*5*). Typical cyclic mechanisms in insects (e.g. flapping flight, tymbal sound production) utilize multiple muscle sets which alternately contract or cuticular structures serving as springs (*22*), whereas the bombardier beetle possesses only valve-opening muscles and the valve is contiguous with flexible structures on all sides (i.e. reservoir chamber and expansion membrane). Hence, valve closure during each pulse cycle likely occurs passively due to mechanical feedback from the explosion, such as dynamic pressure from fluid (hemolymph) displaced by the expansion membrane or impingement of the pressurized expansion membrane directly onto the valve or a combination of both. Simple kinematics models of these scenarios incorporating valve dimensions, the vapor expansion profile, and estimated overpressure discussed above predict forces which are sufficient to close the valve (supplementary online text).

Once the spray pulse is released and the overpressure in the reaction chamber drops, the load on the valve is removed, allowing it to reopen and permit a fresh reactant droplet to enter. It is not known whether the valve-opening muscles contract continually for the duration of spraying or once per pulse cycle, but both scenarios are compatible with passive valve closure and the capabilities of insect muscles (*19*).

The data presented suggest the following mechanism for spray pulsation (Fig. 3). The reservoir chamber musculature contracts for the duration of spraying to apply a continuous pressure to the reactant solution, and the valve muscles also contract, opening the inter-chamber valve and forcing a reactant droplet into the reaction chamber (Fig. 3B). The droplet explodes upon contacting the reaction chamber enzymes (Fig. 3C), producing high-pressure vapor that propels a spray pulse out of the exit channel. Explosion overpressure displaces the expansion membrane and closes the inter-chamber valve, thereby interrupting the flow of reactants. Following the explosion, the pressure in the reaction chamber decreases, the expansion membrane relaxes, the valve reopens, and a fresh reactant droplet enters, starting a new pulse cycle (Fig. 3D). Eventually, the reservoir and valve muscles relax, causing spraying to cease. The exit channel's dorsal membrane relaxes and collapses into its ventral trough, and some quantity of vapor generally remains in the reaction chamber as a pocket surrounded by numerous bubbles (Fig. 3E).

The pulsed spray mechanism of brachinine bombardier beetles is remarkably elegant and effective, protecting these beetles from nearly all predators (and incautious humans). The passive mediation of pulsation by mechanical feedback from the explosion is advantageous as it provides automatic regulation of reactant use. Further, the evolutionary change from a continuous defensive spray (exhibited by close relatives of the brachinines) to a pulsed spray required only relatively minor changes to the reaction chamber inlet structures rather than the evolution of novel valve-closing muscles.

References and Notes:

1. T. Eisner, *J. Insect Physiol.* **2**, 215-220 (1958).
2. D. J. Aneshansley, T. Eisner, J. M. Widom, B. Widom, *Science* **165**, 61-63 (1969).
3. H. Schildknecht, K. Holoubek, K. H. Weis, H. Krämer, *Angew. Chem. Int. Edit.* **3**, 73-82 (1964).
4. M. S. Blum, *Chemical Defenses of Arthropods* (Academic Press, New York, 1981).
5. J. Dean, D. J. Aneshansley, H. E. Edgerton, T. Eisner, *Science* **248**, 1219-1221 (1990).
6. N. Beheshti and A. C. Mcintosh, *Bioinspir. Biomim.* **2**, 57-64 (2007).
7. A. James, K. Morison, S. Todd, *J. R. Soc. Interface* **10**, 20120801 (2013).
8. T. Eisner, D. J. Aneshansley, *Proc. Nat. Acad. Sci. U. S. A.* **96**, 9705-9709 (1999).
9. S. O. Andersen, *Ann. Rev. Entomol.* **24**, 29-61 (1979).
10. T. Eisner, et al., *J. Insect Physiol.* **23**, 1383-1386 (1977).
11. H. Schildknecht, *Angew. Chem. Int. Edit.* **9**, 1-9 (1970).
12. M. W. Westneat, et al., *Science* **299**, 558-559 (2003).
13. J. J. Socha, et al., *BMC Biol.* **5**, doi:10.1186/1741-7007-5-6 (2007).
14. J. J. Socha, et al., *J. Exp. Biol.* **211**, 3409-3420 (2008).
15. M. W. Westneat, J. J. Socha, W.-K. Lee, *Annu. Rev. Physiol.* **70**, 119-142 (2008).
16. W.-K. Lee, J. J. Socha, *BMC Physiol.* **9**, doi:10.1186/1472-6793-9-2 (2009).

17. Materials and methods are available as supplementary materials on *Science* Online.

18. J. F. V. Vincent, J. E. Hillerton, *J. Insect Physiol.* **25**, 653-658 (1979).

19. O. Sotavalta, *Biol. Bull.* **104**, 439-444 (1953).

20. J. F. V. Vincent, U. G. K. Wegst, *Arthropod Struct. Dev.* **33**, 187-199 (2004).

21. J. F. V. Vincent, *Proc. R. Soc. A* **188**, 189-201 (1975).

22. R. F. Chapman, *The Insects: Structure and Function* (Cambridge University Press, Cambridge, UK, ed. 5, 1998).

23. HandBrake, Version 0.9.5, http://handbrake.fr/ (accessed 25 May 2011).

24. FFmpeg, http://www.ffmpeg.org/ (accessed 30 April 2013).

25. W. S. Rasband, ImageJ, Version 1.46a, U. S. National Institutes of Health, Bethesda, MD, USA, http://rsbweb.nih.gov/ij/ (accessed 18 November 2011).

26. F. Álvarez-Padilla, G. Hormiga, *J. Arachnology* **35**, 538-542 (2007).

27. J. Dean, *J. Chem. Ecol.* **5**, 691-700 (1979).

28. M. F. Easton, A. G. Mitchell, W. F. K. Wynne-Jones, *Trans. Faraday. Soc.* **48**, 796-801 (1952).

29. D. L. Camin, F. D. Rossini, *J. Phys. Chem.* **59**, 1173-1179 (1955).

30. R. W. Barnard, K. Pearce, L. Schovanec, *J. Math. Anal. Appl.* **260**, 295-306 (2001).

31. T. Weis-Fogh, *J. Exp. Biol.* **37**, 889-907 (1960).

32. J. M. Gere, *Mechanics of Materials* (Thompson Learning, Ontario, Canada, ed. 6, 2006).

Acknowledgments: Use of the Advanced Photon Source was supported by the U. S. Department of Energy, Office of Science, Office of Basic Energy Sciences, under Contract No. DE-AC02-06CH11357. This work was supported in part by the U. S. Army Research Laboratory and the U. S. Army Research Office through the MIT Institute of Soldier Nanotechnologies under Contract No. W911NF-13-D-0001 and in part by the National Science Foundation through the MIT Center for Materials Science and Engineering under Contract No. DMR-08-19762. This research was funded in part by the U. S. Department of Defense, Office of the Director, Defense Research and Engineering, through the National Security Science and Engineering Faculty Fellowship awarded to C.O. under Contract No. N00244-09-1-0064; in part by the National Science Foundation through funding awarded to W.M. under Contract No. DEB-0908187; and in part by the U. S. Department of Energy, Office of Science, Office of Basic Energy Sciences, under Contract No. DE-SC0012704. All data from these experiments are maintained on a local server.

Fig. 1. *Brachinus elongatulus* pygidial gland morphology. (**A**) Dorsal view. Dashed circle indicates location of pygidial glands. (**B**) Female (top) and male (bottom) pygidial glands: optical micrographs, Chlorazol Black staining (left) and SEM (right). Features are indicated: reservoir chamber (RSC), reaction chamber (RXC), exit channel (EC), and reflector plate (RP). (**C**) Female pygidial glands stained as in B showing rigid (highly sclerotized, brown/tan) and flexible (lightly sclerotized, stained blue) regions. Lightly sclerotized regions are identified: reaction

chamber midline crease (white arrow); junction between reaction chamber and exit channel (purple arrow); exit channel dorsal membrane (yellow arrow). (**D**) False-color SEM showing valve muscles (VM), inter-chamber valve (ICV), and expansion membrane (EM). Other features labeled as in B. Cross-section shown in E is approximately normal to dashed line. (**E**) False-color SEM of cross-section through inter-chamber region. The inter-chamber valve is observed in a closed conformation. Labels and colorization correspond to D, with additional indication for the valve opening (VO).

Fig. 2. Internal dynamics revealed by X-ray imaging. (**A**) First five pulses of a spray; successive frames from 2000-fps video of a male beetle. Scale bar is 200 μm. Location of right reaction chamber (RXC) and exit channel (EC) indicated in frame 4. Right and left exit channels are open starting in frames 4 and 11 respectively. Arrows indicate dramatic displacement of the expansion membrane. Dark objects at left are external debris. (**B**) Reactant droplet (arrow) entering reaction chamber and exploding; successive frames from 2000-fps video of a male beetle. Scale bar is 200 μm.

Fig. 3. Mechanism of spray pulsation. Schematics depict a sagittal section through the middle of a pygidial gland; this perspective is orthogonal to the accompanying X-ray images selected from movies S1 and S2. Scale bars are 200 μm. Reservoir chamber (RSV), reaction chamber (RXC), exit channel (EC), inter-chamber valve (ICV), and expansion membrane (EM) are indicated. (**A**) Gland is inactive. (**B**) Spray initiation. Reactant solution enters through valve. (**C**) Explosion ongoing. Displacement of expansion membrane closes the valve. A spray pulse is ejected. (**D**) Explosion ceases. Expansion membrane relaxes and valve reopens permitting fresh reactant solution to enter. The process repeats C-D-C-D-C-D… with each ‘C-D’ corresponding to one pulse cycle. (**E**) Spraying concluded. The exit channel closes and a vapor pocket remains in the reaction chamber.

Supplementary Materials:

Materials and Methods

Supplementary Text

Author Contributions

References 23-32

Tables S1 and S2

Figures S1-S3

Movies S1-S3

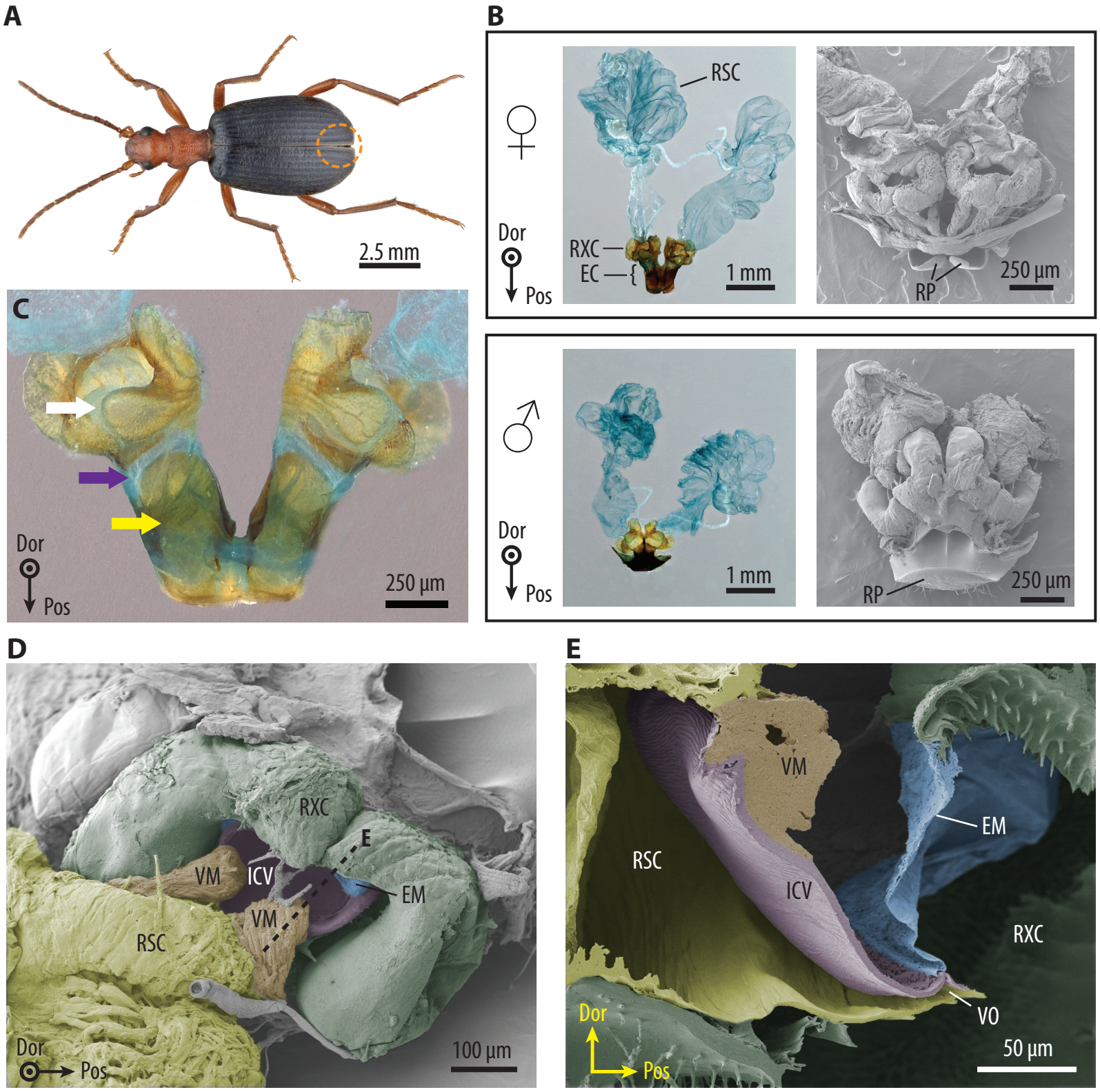
A
2.5 mm
B
RSC
RXC
EC
1 mm
RP
250 µm
Dor
Pos
C
250 µm
D
RXC
E
VM
ICV
EM
RSC
100 µm
E
VM
EM
RSC
ICV
RXC
VO
50 µm

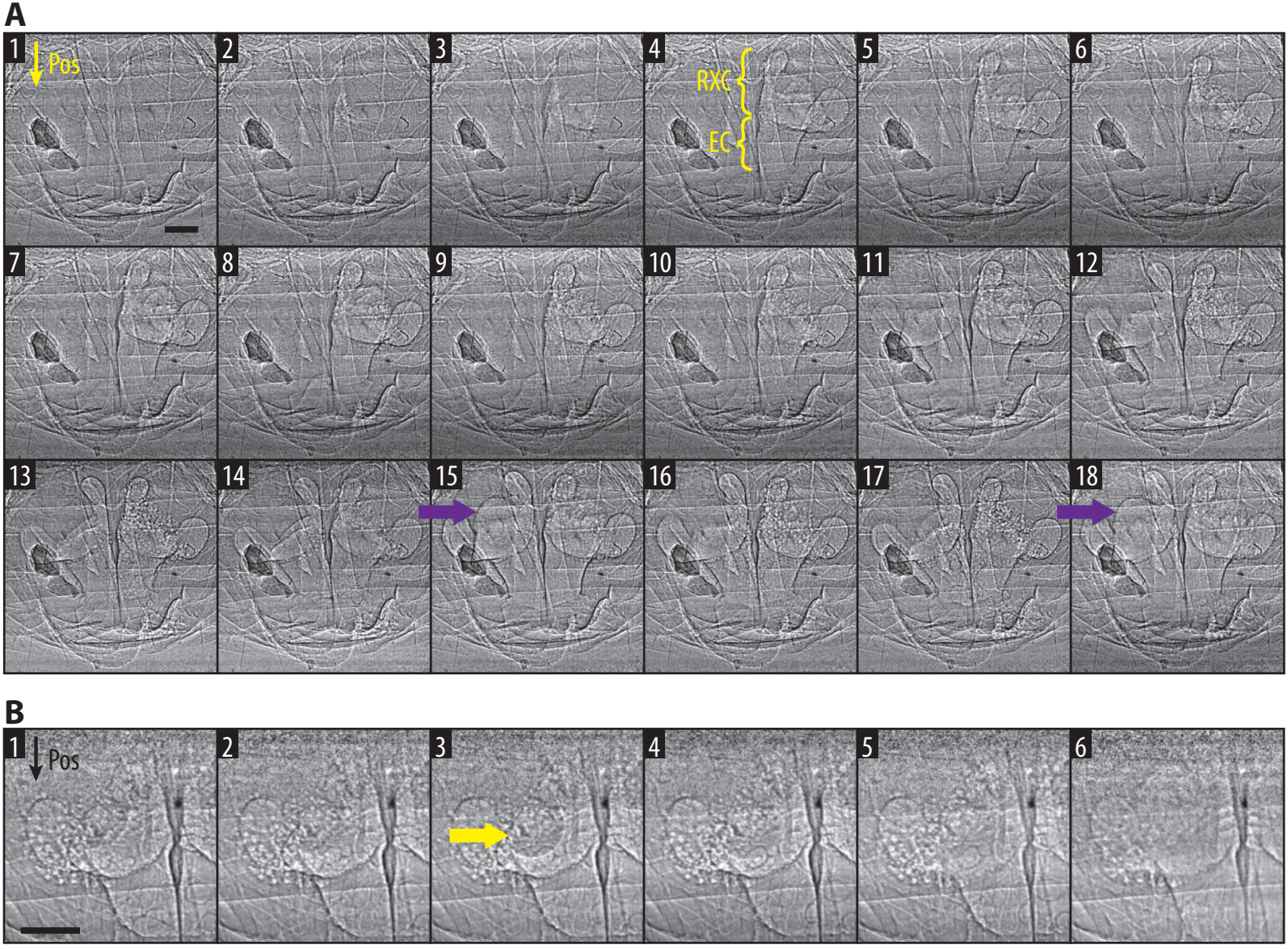
A
1
Pos
2
3
4
RXC
EC
5
6
7
8
9
10
11
12
13
14
15
16
17
18
B
1
Pos
2
3
4
5
6

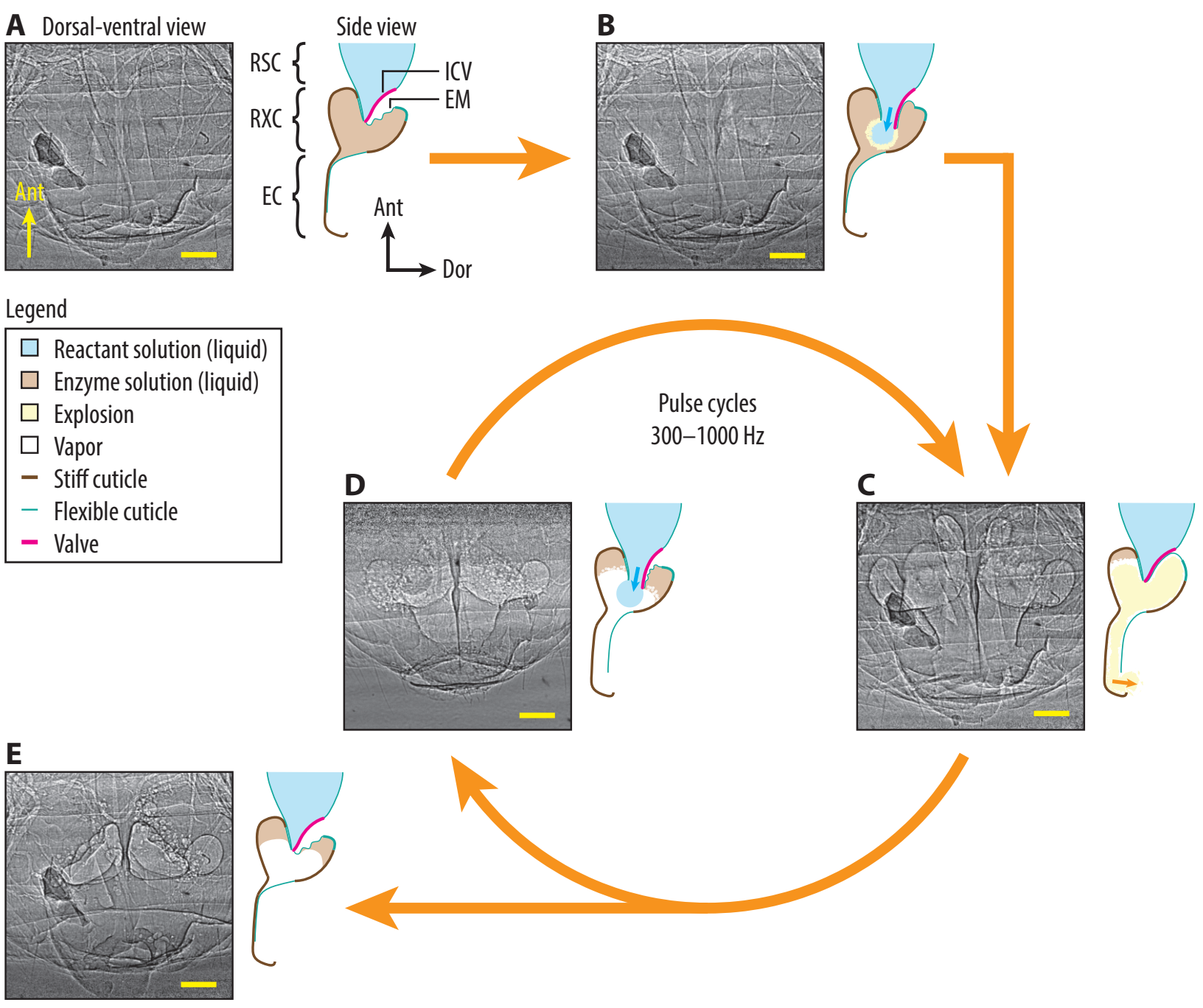
A
Dorsal-ventral view
Ant
Side view
RSC
RXC
EC
ICV
EM
Ant
Dor
B
Legend
Reactant solution (liquid)
Enzyme solution (liquid)
Explosion
Vapor
Stiff cuticle
Flexible cuticle
Valve
Pulse cycles
300–1000 Hz
C
D
E

Supplementary Materials for

Mechanistic Origins of Bombardier Beetle (Brachinini) Explosion-Induced Defensive Spray Pulsation

Eric M. Arndt, Wendy Moore, Wah-Keat Lee, Christine Ortiz

correspondence to: cortiz@mit.edu

This PDF file includes:

Other Supplementary Materials for this manuscript includes the following:

Materials and Methods

Beetle Collection and Care

Live *Brachinus elongatulus* were collected at night in a dry creek bed in Madera Canyon near Green Valley, AZ, or from along the banks of the San Pedro River several miles west of Tombstone, AZ. Beetles were maintained prior to the experiments with free access to water, food, and shelter. After the experiments, beetles were euthanized with ethyl acetate or ethanol and then preserved in 90% ethanol solution.

Synchrotron X-ray Imaging

Synchrotron X-ray phase-contrast imaging was performed at the XOR-32ID undulator beamline of the Advanced Photon Source at Argonne National Laboratory (Argonne, IL, USA). X-ray energy was selected using a Si-111 double-crystal monochromator and flux was adjusted by changing the undulator gap. The source-to-sample distance was 65 m. X-rays transmitted by the sample were converted to visible light by a cerium-doped yttrium aluminum garnet scintillator for detection with a video camera. In early experiments (Aug-2010, 30 and 250 fps), the beetle-mounting setup comprised a metal strip clamped to the end of a horizontal rod, which was itself clamped to a vertical post on an optical table. A stop was placed on the post so that the horizontal assembly could be removed and then quickly returned to the same height. In later experiments (Mar-2013, 1000 and 2000 fps), the mounting setup comprised a metal plate bearing a hole along the midline. The plate was screwed to a metal frame at its corners, and this frame was affixed to a vertical post attached to an optical table.

In preparation for imaging, a beetle was anesthetized by placement in a laboratory freezer or in a vial placed in an ice-filled container. Beetles sometimes discharged during chilling. Once immobile, the beetle was mounted with a "collar" of modeling clay, either to the metal strip with its abdomen protruding below (in early experiments) or to the metal plate with its abdomen tip placed over the hole (in later experiments). In the early experiments, the horizontal rod bearing the metal strip was removed from the vertical post and placed on a table to mount the beetle and then returned to its previous configuration. In later experiments, the mounting assembly was kept fixed in place. Mounting was accomplished by pressing a strip of modeling clay across the midsection of the beetle while it laid ventral-side-up on a table, then lifting the clay and beetle and placing in the desired position on the mounting apparatus, and then pressing the clay firmly onto the metal on either side of the beetle to cause it to stick. In some cases, an ice pack was used to chill the modeling clay and the table where the beetle was handled in an attempt to delay the beetle's waking. The mounting setup was pre-positioned to place the abdomen tip approximately in line with the X-ray beam, and in the case of the metal plate a piece of tape placed across part of the hole was used to aid alignment. For a few tests, beetles were mounted upside down to test the effect of gravity on vapor pocket shape and position (no effect was observed); beetle 12 in Tables S1 and S2 was mounted in this fashion. Occasionally, beetles awoke during handling and mounting, and these were either re-anesthetized for remounting or, if they discharged, returned to a separate container and imaged at a later time. After securing the experimental hutch, the beetle was monitored by closed-circuit television. When the beetle started to wake and move its legs, the X-ray stutter was opened. Typically the beetle panicked upon waking,

presumably due to a combination of confinement by the clay and irritation from the X-ray beam; these conditions produced the best chances of observing a spray. If the beetle did not spray immediately, it was poked repeatedly using a sharp object (such as a pin) attached to a remotely controlled positioning stage. If a spray was observed, the camera was stopped manually. In some cases, multiple imaging trials were conducted for a single beetle, but in no case was a spray recorded after the first trial, and only first trials are considered in the statistical analyses.

Imaging at 30 fps was performed under conditions similar to those described in the literature (*12*-*16*) with 25-keV X-rays, a 1-m sample-to-detector distance, and a flux of approximately 2×10^{10} photons/s/mm^2. Video was recorded onto a MiniDV tape using a Cohu 2700 video camera (San Diego, CA, USA) coupled to a 2× microscope objective and tube lens, providing a field of view of roughly 3.2 mm by 2.4 mm (708×480 pixels). The video (in DV format) was transferred to computer using a video tape deck and Apple iMovie software (Cupertino, CA, USA). The DV file was converted first to MP4 format and then to a TIFF image stack using the free open-source software HandBrake (*23*) and FFmpeg (*24*), respectively. Movies of the discharges were created from the TIFF files and saved in AVI format (30-fps playback, no compression) using ImageJ (*25*).

Imaging at 250 fps was performed using the same beam energy and sample-to-detector distance as for 30-fps imaging, but with a higher X-ray flux. A Photron Fastcam SA1.1 model 675K-M1 high-speed camera (Tokyo, Japan) coupled to a 5× microscope objective and tube lens was used for the detector. The theoretical field of view was 4.1 mm by 4.1 mm, though the usable field of view was reduced somewhat vertically by the size of the beam, and the pixel size was 4.0 μm (verified using calibration images taken of a 400-mesh TEM grid). The camera ran continuously until stopped manually when a discharge was observed, and its 8-GB internal memory held 21.8 s (5457 frames) of 250-fps 1024×1024 video. Each video was downloaded from the camera as TIFF image stacks which were later adjusted for brightness and contrast in ImageJ. Movies of the discharges were exported from ImageJ as AVI files (25-fps playback, JPEG compression).

Imaging at 1000 fps and 2000 fps was performed using 18-keV X-rays, a sample-to-detector distance of approximately 60 cm, and a much higher flux (the maximum output of the undulator source at this beam energy, on the order of 10^{13} photons/s/mm^2). The undulator gap was 15.531 mm with a 0.2-mm taper. The same camera and optics were used as for 250-fps imaging, giving the same theoretical field of view and pixel size (again verified by calibration images of a 400-mesh TEM grid). However, the usable field of view was greatly reduced due to the smaller size of the beam (necessary to reduce the thermal load on the beamline optics), especially in the vertical dimension. The camera ran continuously as before, and its internal memory held 5.46 s and 2.73 s of 1000- and 2000-fps 1024×1024 video, respectively. The image stacks were background-corrected, normalized, and smoothed using a custom script in Matlab (MathWorks, Natick, MA, USA). Movies of the discharges were exported from ImageJ as AVI files (25-fps playback, JPEG compression). Movies S1-S3 were converted to MOV files (25-fps playback, h264 compression) using FFmpeg.

Statistical analysis was generally performed using Microsoft Excel software (Redmond, WA, USA). The calculations for Fisher's exact test were done using a Texas Instruments TI-89 calculator (Dallas, TX, USA) due to difficulties in calculating large factorials in Excel.

Optical Microscopy

For optical microscopy shown in Fig. 1, following excision of the pygidial glands from the beetles' abdomens, non-cuticular tissue surrounding the glands was digested and cleared using a pancreatin solution as described by Álvarez-Padilla and Hormiga (*26*). Non-sclerotized regions of the glands, which were colorless prior to staining, were stained blue with Chlorazol Black E to increase contrast. The glands were imaged using a Visionary Digital BK Plus imaging system (http://www.visionarydigital.com), and images from multiple focal planes were combined using Zerene Stacker software (Richland, WA, USA).

Scanning Electron Microscopy

For scanning electron microscopy shown in Fig. 1 (except E), *B. elongatulus* which had been preserved in 90% ethanol solution were dissected in air with the aid of an Olympus SZX16 stereomicroscope (Tokyo, Japan). The pygidial gland assembly was temporarily stored in 95% ethanol solution and then dehydrated through graded ethanol (10 minutes each of 98% and 2× 100%). The glands were picked up in a glass Pasteur pipet and transferred to a piece of filter paper to air-dry. With the aid of the stereomicroscope, the glands were mounted on an aluminum stub using double-sided carbon tape. The glands were sputter-coated with gold-palladium for 120 s at 50 mA utilizing sample rotation with a Denton Vacuum Desk V coater (Moorestown, NJ, USA). Imaging was conducted on a JEOL 6700F field-emission scanning electron microscope (Tokyo, Japan) using an accelerating voltage of 5 kV, an emitter current of 10 μA, and a nominal working distance of either 8 or 15 mm, and images were collected using a low-angle secondary-electron detector.

The female *B. elongatulus* gland shown in Fig. 1E was sectioned by the following procedure. After excision from a freshly sacrificed beetle and subsequent storage in 75% ethanol, the gland was dehydrated through a graded ethanol series (10 min. each of 80%, 90%, 95%, and 3× 100%) and then transferred to toluene through a graded series (15 min. each of 2:1 ethanol-toluene, 1:2 ethanol-toluene, and 2× 100% toluene). An embedding solution (ES) was prepared by dissolving polystyrene (M_w = 350,000 g/mol, melt index 3.4; Sigma Aldrich) in toluene at 10 w/v% concentration. The gland was transferred to ES through a graded series (45 min. each of 2:1 toluene-ES and 1:2 toluene-ES followed by 90 min. of 100% ES). The gland was picked up in a glass Pasteur pipet and transferred to the tip of a BEEM #3 embedding capsule, the lid of which had been perforated using sharp-tipped forceps. ES was added to fill the capsule, and the capsule lid was attached. The capsule was placed upright in a capsule holder in a fume hood for several days in order for the toluene to slowly evaporate to harden the polystyrene. Once the block had hardened, general-purpose epoxy was poured into the capsule to fill (to compensate for the considerable shrinkage during drying) in order to obtain a block of sufficient length to fix in a microtome chuck. The epoxy was allowed to harden at room temperature. The block was cut from the capsule using a razor blade. Microtome sectioning of the block face to reveal the gland interior was performed using a Leica EM UC6 ultramicrotome (Wetzlar, Germany). Thick sections were cut on a Diatome Histo diamond knife (Hatfield, PA, USA), into a water trough at room temperature, until roughly half of the gland remained. The block was placed in toluene overnight to dissolve the polystyrene

embedment. Once de-embedded, the gland was transferred by pipet to a glass vial. The gland was washed in two changes of toluene (10 min. each) and then transferred to ethanol through a graded series (10 min. each of 2:1 toluene-ethanol, 1:2 toluene-ethanol, and 2× 100% ethanol). The gland was transferred by pipet to a piece of filter paper to air dry and then mounted for SEM, coated with gold-palladium, and imaged using the previously described procedures.

False-colorization of the scanning electron micrographs in Fig. 1D,E was performed using Adobe Photoshop CS6 software (San Jose, CA, USA).

Supplementary Text

Elicitation of Sprays

Previous studies of bombardier beetles have typically relied on the experimenter to manually elicit sprays (e.g. by pinching the beetles' legs with forceps), but synchrotron X-ray imaging restricted us to remote specimen manipulation due the high radiation levels present. We found that restraining beetles with modeling clay would occasionally cause them to spray upon awaking from cold-induced anesthesia, with irritating effects of the X-ray beam (*13*) possibly providing further aggravation. All of the sprays recorded at higher imaging rates (1000 and 2000 fps) occurred in this manner. In earlier tests at lower frame rates (30 and 250 fps), a sharp pin attached to a motorized stage was used to poke the beetles if they did not spray immediately, and this method gave some success, but poking was ineffective at the very high X-ray fluxes necessary for higher-rate imaging due to the time required to align the pin and prod the beetle exceeding the brief period before X-ray damage becomes significant. No sprays were recorded after the onset of visible X-ray effects (e.g. leg twitching, protrusion of the aedeagus in males, bowel eversion), the occurrence and timing of which depended on the imaging conditions.

Differences between Aug-2010 and Mar-2013 Experiments

The percentage of beetles recorded spraying relative to the number of beetles tested was higher in the initial set of experiments (Aug-2010) at lower imaging rates than in the later set (Mar-2013) at higher frame rates (40.0% for 10 beetles imaged at 30 or 250 fps vs. 7.75% for 129 beetles imaged at 1000 or 2000 fps), and this discrepancy is greater than what would be expected purely by chance ($p = 0.0088$, Fisher's exact test). Multiple factors must be considered to interpret this observation and its possible causes. The beetles were collected at different times and in different locations, so inherent behavioral differences may exist between the two populations. However, the differences in imaging conditions between the two sets of experiments are most likely the dominant factor. Lower X-ray fluxes and higher X-ray energies (which are less readily absorbed by tissue) were used in the first set of experiments, resulting in lower expected rates of radiation-induced damage per unit volume of tissue compared to later experiments. Correspondingly, more time was available for the beetle to spray, spontaneously or as a result of poking, before radiation effects grew pronounced. Additionally, in the earlier experiments, 5 sprays from 2 beetles (over half of those recorded then) occurred while poking, with two of the sprays (both by beetle 1 in Table S1) clearly aimed at the pin as observed in concurrent visible-light video.

X-ray Effects on Live Beetles

For imaging at 30 fps, using the optimized settings as reported in (*13*) and illuminating only the animals' abdomens, no X-ray effects were observed even after many minutes of imaging. For imaging at 250-fps, however, the much higher fluxes used resulted in observable radiation effects (leg twitching, gut eversion, and aedeagus protrusion) after only a few minutes of exposure. The fluxes used for 1000- and 2000-fps imaging were higher still, but a much smaller region of the abdomen was illuminated due to the significantly smaller vertical extent of the beam. No externally apparent X-ray effects were noted for these beetles, which would scurry around in normal fashion after imaging. Increased survivorship for abdomen-only irradiation in insects has been noted in previous studies (*13*). However, in all but a handful of cases, beetles could be handled with impunity after only a short period (<1 minute) of beam exposure at these fluxes, suggesting that the irradiation of their pygidial glands typically rendered them unable to spray, possibly due to damage to the muscles and nerves which control them; this effect likely contributed to the lower success rates relative to the Aug-2010 experiments. It is unknown whether these beetles would have eventually died due to radiation poisoning, as they were typically euthanized at the end of each day. However, a set of beetles imaged at 1000 or 2000 fps that were not euthanized until the end of the experiments (this group included the beetles had been recorded spraying) all survived up to that point, which was up to two days following irradiation.

Spray Durations

Spray durations, as determined from X-ray video, ranged from 5.0 ± 0.5 ms to 344 ± 4 ms, with the median duration being 23.5 ms and 80% of the discharges lasting 40 ms or less (Table S1). On the whole, spray durations were lengthier than those reported for *S. insignis* (*5*)—in some cases, considerably so—but it is unclear whether this represents a fundamental difference between the two species or differences in experimental conditions. We also find that spray durations often vary considerably between consecutive discharges from the same beetle, suggesting that physical characteristics such as the size or shape of the pygidial glands do not fix the duration. Rather, it would appear that the beetle exercises control over spray duration, which could be a means of tuning its defensive response to a wide variety of potential predators to ensure effective deterrence while conserving reactants and enzymes.

Spray Pulsation Rates

Pulses were sufficiently distinct in 2000-fps X-ray video that average spray pulsation rates were quantifiable (Fig. S1, Table S2), and these values ranged from 341-976 Hz (median, 667 Hz; mean ± SD, 698 ± 146 Hz). These analyses exclude data from beetle 14 in table S1; of this beetle's two recorded sprays, the first comprised only a single pulse; and the second was highly irregular, with vapor back-flowing into the reservoir chamber with each pulsation cycle so that the reservoir partially filled with vapor, impeding the injection of reactants and causing pulsation to be dramatically slower than observed in other beetles. As shown in Fig. S1B, average pulsation rate does not obviously correlate with the gland active time suggesting no tendency of sprays with greater or lesser pulsation rates towards longer or shorter durations, or vice-versa. For individual beetles, average pulsation rates did not vary significantly between glands or successive sprays. In addition, qualitatively, pulsation appeared to be quite regular rather

than increasing or decreasing in rate. Overall, average pulsation rates were similar to those reported in (*5*) for *S. insignis* but higher on average and showing wider variation.

Exit Channel Opening/Closing

The ability for the exit channel to open and close is due to its membranous dorsal part, which is readily displaced by the exiting spray to form an open channel when the gland is active. When pulsation stops at the conclusion of gland activity, the dorsal membrane collapses into the trough of the exit channel, displacing vapor from the exit channel and causing the exit channel to disappear from view in the X-ray video (Movies S1-S3). This relaxation occurs slowly (median closure time, 12.0 ms; range, 2.5-86.5 ms) compared to the timescale of a pulse cycle (~1-3 ms).

One-Gland versus Two-Gland Sprays

Two-gland sprays were very common in our experiments, comprising 80% of those we recorded (Table S1); it is unclear if this preference is a response to the specific procedures we employed or is a more general behavior. This ability to use the pygidial glands independently gives the beetle an additional method (other than adjusting spray duration) of tailoring its defensive response to the perceived threat and also provides redundancy should one of its glands lack sufficient reactants or enzymes to function. For two-gland sprays, glands typically did not become active simultaneously. The median offset between the start of activity in the two glands was 3.5 ms (range, 0-18 ms). This second-gland start delay is an order of magnitude shorter than the beetles' defensive reaction time as reported by Dean (*27*), suggesting that it is due to physiological limitations in synchronizing the start of gland activity rather than conscious control by the beetle. In contrast, once both glands are active, their pulsation is roughly synchronous, and activity typically ceases almost simultaneously in both glands at the conclusion of spraying.

Reaction Chamber Vapor Pockets

X-ray imaging revealed the frequent presence of vapor pockets inside quiescent beetles which appear as bright, rounded features with edges enhanced by phase contrast. The positions of the vapor pockets are generally consistent with being internal to the reaction chambers, even reflecting conformational differences between females and males which are apparent in excised pygidial glands, indicating that the vapor pockets are located within the reaction chambers. Such vapor pockets were quite common, being observed in roughly two-thirds of the beetles we imaged, and their presence did not obviously impede the beetles' ability to spray. The size and shape of the vapor pockets varied from beetle to beetle, and between glands of individual beetles, but typically conformed to a few motifs (e.g. ovoid, heart-shaped, or bi-lobular similar to the reaction chamber). This variation does not reflect differences in the sizes and shapes of the reaction chambers but rather in the portion of their volume that is occupied by vapor, the balance being enzyme solution (liquid). Presumably, while the gland is inactive, fresh enzyme solution is synthesized and transported to the reaction chamber, where it gradually displaces vapor (which could be passively released from the exit pore), until the reaction chamber once again becomes completely liquid-filled given sufficient recharging time. Rarely, vapor pockets were also observed in reservoir chambers; this may be due to

leakage of either vapor or enzyme solution from the reaction chamber into the reservoir through the inter-chamber valve, as was observed during spray 2 from beetle 14 in Table S1.

Behavioral Differences between Females and Males

The differences in pygidial gland morphology between females and males (Fig. 1B) raise the question of what other differences might exist between the sexes. In fact, our experiments suggest that defensive behavior does differ somewhat between *B. elongatulus* females and males. Previous studies of bombardier beetles have rarely distinguished between the sexes and none have systematically looked for sex-specific differences in the defensive mechanism, whereas our experiments were conducted with comparable numbers of females and males. The percentage of females tested that we recorded spraying was much less than that of males (4.35% of 69 females vs. 15.7% of 70 males, $p = 0.019$, Fisher's exact test), suggesting that females are less likely to spray or require a greater perceived threat to do so. Moreover, female sprays tended to be longer in duration than male discharges, as reflected in their median durations (68.8 ms for 6 female sprays vs. 20.8 ms for 24 male sprays), which supports the idea that the females typically sprayed in response to a greater perceived threat. It is not clear if the sexual dimorphism of the pygidial glands relates to these behavioral differences, although the wider separation of the pygidial glands in females as compared to males might provide more efficient cooling and thereby permit longer discharges.

However, females and males did share some important similarities. For beetles recorded discharging, the average number of recorded sprays per beetle was not statistically different between females and males (2.00 vs. 2.18 respectively, $p = 0.82$, two-tailed unpooled t-test). Average spray pulsation rates were also similar between the single female and several males recorded spraying at 2000 fps (679 Hz vs. 700 Hz, respectively, $p = 0.53$, two-tailed unpooled t-test), suggesting that despite sexual differences in exit pore configuration, the pulsation mechanism operates fundamentally the same in both sexes. Finally, both sexes showed the ability to spray with either one defensive gland alone or both glands simultaneously.

Reactant Droplet Mass

Using the average volume calculated for the reactant droplets observed in Movie S2 (4.7 ± 0.5 nL), the composition of the reactant solution (*3*, *10*), and component densities (*28*, *29*), and making a simplifying assumption that the *p*-hydroquinones behave ideally in solution, an average droplet mass is calculated as:

$$m_{HP} = 0.25m_{tot} \quad ; \quad m_{HQ} = 0.1m_{tot} \quad ; \quad m_{PD} = 0.1m_{tot} \quad ; \quad m_{W} = 0.55m_{tot}$$

$$\left.\begin{aligned} \frac{m_{PD}}{m_{HP} + m_{HQ} + m_{W}} &= \frac{0.1m_{tot}}{0.25m_{tot} + 0.1m_{tot} + 0.55m_{tot}} = 0.11 \\ \frac{m_{PD}}{m_{HP} + m_{HQ} + m_{W}} &= \frac{\rho_{PD}V_{PD}}{m_{HQ} + \rho_{HP+W}V_{HP+W}} \end{aligned}\right\} \rightarrow \rho_{PD}V_{PD} = 0.11\left(m_{HQ} + \rho_{HP+W}V_{HP+W}\right) \qquad (1)$$

$$\left.\begin{aligned} \frac{m_{HP} + m_{W}}{m_{HQ}} &= \frac{0.25m_{tot} + 0.55m_{tot}}{0.1m_{tot}} = \frac{0.8m_{tot}}{0.1m_{tot}} = 8 \quad \rightarrow \quad m_{HP} + m_{W} = 8m_{HQ} \\ m_{HP} + m_{W} &= \rho_{HP+W}V_{HP+W} \end{aligned}\right\} \rightarrow V_{HP+W} = \frac{8m_{HQ}}{\rho_{HP+W}}$$

(continued below)

$$V_{tot} - V_{HP+W} = V_{PD}$$

$$\rho_{PD}\left(V_{tot} - V_{HP+W}\right) = \rho_{PD}V_{PD} = 0.11m_{HQ} + 0.11\rho_{HP+W}V_{HP+W}$$

$$\rho_{PD}V_{tot} = 0.11m_{HQ} + \left(0.11\rho_{HP+W} + \rho_{PD}\right)V_{HP+W}$$

$$\rho_{PD}V_{tot} = 0.11m_{HQ} + \left(0.11\rho_{HP+W} + \rho_{PD}\right)\left(\frac{8m_{HQ}}{\rho_{HP+W}}\right)$$

$$\rho_{PD}V_{tot} = 0.11m_{HQ} + \frac{0.89\rho_{HP+W}m_{HQ}}{\rho_{HP+W}} + \frac{8\rho_{PD}m_{HQ}}{\rho_{HP+W}}$$

$$\rho_{PD}V_{tot} = \left(1 + \frac{8\rho_{PD}}{\rho_{HP+W}}\right)m_{HQ} \quad \rightarrow \quad m_{HQ} = \frac{\rho_{PD}V_{tot}}{\left(1 + \frac{8\rho_{PD}}{\rho_{HP+W}}\right)} = \frac{V_{tot}}{\frac{1}{\rho_{PD}} + \frac{8}{\rho_{HP+W}}}$$

$$\left.\begin{aligned} V_{tot} &= 4.7 \pm 0.5 \text{ nL} \\ \rho_{PD} &= 0.77 \text{ g/mL} \\ \rho_{HP+W} &= 1.1 \text{ g/mL} \end{aligned}\right\} \rightarrow m_{HQ} = \frac{\left(4.7 \pm 0.5 \text{ nL}\right)}{\frac{1}{\left(0.77 \text{ g/mL}\right)} + \frac{8}{\left(1.1 \text{ g/mL}\right)}} \times \frac{1 \text{ mL}}{10^{6} \text{ nL}} \times \frac{10^{6} \ \mu\text{g}}{1 \text{ g}} = 0.55 \pm 0.06 \ \mu\text{g}$$

$$m_{HQ} = 0.1m_{tot} \quad \rightarrow \quad m_{tot} = 10m_{HQ} = 10\left(0.55 \pm 0.06 \ \mu\text{g}\right) = \boxed{5.5 \pm 0.6 \ \mu\text{g}} \quad \text{Mass of reactant droplet} \qquad (2)$$

Spray Pulse Mass

The mass of a spray pulse is expected to be the sum of the mass of the reactants that produced it (i.e. the mass of the reactant droplet) and of some quantity of enzyme solution that is ejected concomitantly. The first pulse from each gland in Fig. 2A, where both reaction chambers are initially completely filled with enzyme solution, results in a vapor pocket which fills most of the reaction chamber, demonstrating that large quantities of enzyme solution can be ejected. However, for subsequent pulses, the maximum size of

the vapor pockets remains consistent, suggesting that no significant amounts of enzyme solution are ejected after the first pulse, i.e. that the spray pulsation mechanism reaches a steady-state condition where reactant mass inflow equals spray pulse mass outflow, and therefore the mass of a spray pulse can be taken to equal that of a reactant droplet.

However, besides the enzyme solution initially present in the reaction chamber, some quantity of enzyme solution is likely present in the enzyme secretory network (*11*), and this could contribute to the spray pulse mass by draining into the reaction chamber between pulses. As described by Schildknecht (*11*), the enzyme secretory network consists of numerous tubules, which are about 1 μm in diameter and several tens of micrometers in length, that connect secretory cells outside the reaction chamber to pores in the reaction chamber wall, and this description is consistent with our SEM observations. If we take 100 μm for the tubule length (i.e. an upper estimate), then the volume per tubule is of order $(10^{-6}$ m)(10^{-6} m)$(10^{-4}$ m) = 10^{-16} m^3, or 0.1 pL. The total number of tubules has not been thoroughly characterized, but SEM imaging suggests order 10^3 to be a reasonable estimate, so that the estimated total volume of the enzyme secretory network is of order 10^{-13} m^3, or 0.1 nL. This value is small compared to the volume of a reactant droplet (~5 nL), and assuming the densities of reactant solution and enzyme solution are each ~1 g/cm^3, the total mass of enzyme solution present in the secretory network is therefore not significant compared to the mass of a reactant droplet. Although the rate of enzyme synthesis and secretion in bombardier beetles has not been studied, secretion of newly synthesized enzyme solution into the reaction chamber must occur fairly slowly, since the size of vapor pockets inside quiescent reaction chambers was observed to be stable during X-ray imaging (i.e. for at least multiple minutes); thus, enzyme solution synthesized by the secretory cells while spraying is also not expected to meaningfully contribute to the spray pulse mass. Therefore, the spray pulse mass can be reasonably approximated as the reactant droplet mass once the maximum vapor pocket size has reached a steady state.

Average Overpressure in the Reaction Chamber and Estimated Tensile Stress in the Reaction Chamber Walls

The time-average overpressure in the reaction chamber during the process of spray acceleration (i.e. from explosion initiation until the spray pulse exits the beetle, during which time the explosion overpressure can perform work on the spray) is calculated by equating the kinetic energy of the spray pulse (3×10^{-7} J) to pressure-volume work. The kinetic energy of the spray pulse is calculated by assuming a 10 m/s spray velocity (*5*) where the sprass pulse mass equals the reactant droplet mass. For purposes of calculation, the reaction chamber and exit channel are approximated as a cylinder of radius 100 μm (corresponding to the radius of the exit channel; see Figs. 1 and 2) and length 500 μm (corresponding to the distance from the valve opening to the exit channel opening; see Figs. 1 and 2), and the explosion gasses at average overpressure P_{over} expand through the volume of this cylinder. The average overpressure is calculated as:

$$K_{\text{spray}} = P_{\text{over}}\Delta V = P_{\text{avg}}\left(\pi r^2 l\right) \quad \rightarrow \quad P_{\text{over}} = \frac{K_{\text{spray}}}{\pi r^2 l}$$
$$P_{\text{over}} = \frac{\left(3\times10^{-7}\ \text{J}\right)}{\pi\left(1\times10^{-4}\ \text{m}\right)^2\left(5\times10^{-4}\ \text{m}\right)} = 2\times10^{4}\ \text{Pa} = \boxed{20\ \text{kPa}} \tag{3}$$

The overpressure will produce a tensile stress in the reaction chamber wall. To estimate an upper limit for the average tensile stress over the duration of a pulse, a cylindrical hoop of radius 200 µm (corresponding to the roughly 400-µm maximum diameter of the reaction chamber) and wall thickness 3 µm (estimated from morphological studies) is considered. The tensile stress is estimated as:

$$\sigma_{\text{wall}} = \frac{P_{\text{over}} r}{t} = \frac{\left(2\times10^{4}\ \text{Pa}\right)\left(2\times10^{-4}\ \text{m}\right)}{\left(3\times10^{-6}\ \text{m}\right)} = 1\times10^{6}\ \text{Pa} = \boxed{1\ \text{MPa}} \tag{4}$$

Time Scale and Magnitude of Spray Acceleration

The time during which the spray pulse accelerates from the droplet injection velocity (i.e. that at which the droplet enters the reaction chamber) to the exit velocity of 10 m/s (*5*) can be calculated with knowledge of the distance over which this acceleration occurs, which is estimated as 500 µm. For purposes of calculation, the droplet injection velocity is estimated as one droplet diameter (~200 µm) divided by one frame duration (0.5 ms), giving a value of 0.4 m/s which is negligible compared to the exit velocity. The time scale of spray pulse acceleration is calculated as:

$$\Delta v = v_{\text{spray}} - \cancel{v_{\text{inject}}} = at$$
$$l = \frac{at^2}{2} = \frac{\left(\Delta v\right)t}{2} \approx \frac{v_{\text{spray}}t}{2} \quad \rightarrow \quad t = \frac{2l}{v_{\text{spray}}} \tag{5}$$
$$t = \frac{2\left(5\times10^{-4}\ \text{m}\right)}{\left(10\ \text{m/s}\right)} = 1\times10^{-4}\ \text{s} = \boxed{0.1\ \text{ms}}$$

From this value, the average acceleration is calculated as:

$$a = \frac{v_{\text{spray}}}{t} = \frac{\left(10\ \text{m/s}\right)}{\left(1\times10^{-4}\ \text{s}\right)} = \boxed{1\times10^{5}\ \text{m/s}^2} \approx 10000\ g \tag{6}$$

Extension Ratios of the Expanded Expansion Membrane

The relaxed expansion membrane dimensions are measured from X-ray (Fig. 2A frame 14) and SEM (Fig. 1E) images as illustrated in Fig. S2A,C. Additionally, the maximum length of the stretched expansion membrane in the coronal plane is measured from Fig. 2A frame 15 as shown in Fig. S2B. To obtain dimensions for the expansion membrane at maximum expansion, the expanded expansion membrane will be considered

to be a hemi-ellipsoid. This assumption is consistent with the hemi-elliptical cross-section observed in the X-ray images (e.g. Fig. 2A frame 15). Fig. S2 defines an *xyz* coordinate system coincident with the ellipsoid axes which will be referenced in the proceeding discussion. The *x* and *y* semi-axes of the hemi-ellipse are estimated as 190 μm and 160 μm as shown in Fig. S2B. The *z* semi-axis is taken to be the maximum spacing between sclerotized cuticles in the inter-chamber region as shown in Fig. S2C. The hemi-ellipsoid thus occupies a volume that is schematized by the magenta shading in Fig. S2C,D. Considering an expansion membrane volume element located at the apex of the hemi-ellipsoid and assuming affine deformation, the extension ratio in the *y* direction, λ_y, is estimated as the ratio of the stretched and relaxed lengths measured in Fig. S2A,B:

$$\lambda_y = \frac{l_y}{l_{y0}} = \frac{(560\ \mu\text{m})}{(340\ \mu\text{m})} = \boxed{1.6} \tag{7}$$

To calculate the extension ratio in the *z* direction, the stretched length is estimated as one half of the perimeter of the ellipse with the same *x* and *z* semi-axes as the hemi-ellipsoid; this perimeter is calculated from the hypergeometric series F(-½, ½; 1; χ^2) (*30*) in Matlab. The extension ratio λ_z is estimated as the ratio of this value to the relaxed length measured in Fig. S2C:

$$\begin{aligned}
&\chi = \frac{(190\ \mu\text{m}) - (90\ \mu\text{m})}{(190\ \mu\text{m}) + (90\ \mu\text{m})} = 0.357 \\
&\chi^2 = 0.128 \quad \rightarrow \quad \text{F}\left(-1/2, -1/2\,;\ 1\,;\ \chi^2\right) = 1.03 \\
&l_z = \frac{1}{2} \times \left[\pi \left((190\ \mu\text{m}) + (90\ \mu\text{m}) \right) (1.03) \right] = 450\ \mu\text{m} \\
&\lambda_z = \frac{l_z}{l_{z0}} = \frac{(450\ \mu\text{m})}{(160\ \mu\text{m})} = \boxed{2.8}
\end{aligned} \tag{8}$$

If the expansion membrane material is considered to be incompressible, then the extension ratio in the *x* direction can be estimated as:

$$\lambda_x \lambda_y \lambda_z = 1 \quad \rightarrow \quad \lambda_x = \frac{1}{\lambda_y \lambda_z} = \frac{1}{(1.6)(2.8)} = \boxed{0.22} \tag{9}$$

Kinematics of the Fluid Displaced by the Expansion Membrane

In order for the expansion membrane to expand outwards, it must displace hemolymph in the body cavity of the beetle. The kinetic energy of the fluid (hemolymph) displaced by the expansion membrane can be estimated as equal to the work done by the pressurized gasses in the reaction chamber expanding through the hemi-ellipsoidal volume included by the expanded expansion membrane. Here, the work done stretching the expansion membrane is neglected; although an accurate estimate of the strain energy is not possible without further knowledge of the expansion membrane materials properties, due to the membrane's thinness and the extreme compliance exhibited by such

extensible cuticles, the amount of strain energy is expected to be relatively small compared to the available amount of pressure-volume work. The inertia of the expansion membrane is also neglected. The kinetic energy imparted to the displaced fluid is estimated as:

$$K = P_{\text{over}}\Delta V = P_{\text{over}}V_{\text{hemi}}$$
$$V_{\text{hemi}} = \frac{2}{3}\pi\left(1.9\times10^{-4}\ \text{m}\right)\left(1.6\times10^{-4}\ \text{m}\right)\left(9.0\times10^{-5}\ \text{m}\right) = 5.7\times10^{-12}\ \text{m}^3 = 5.7\ \text{nL} \qquad (10)$$
$$K = \left(2\times10^{4}\ \text{Pa}\right)\left(5.7\times10^{-12}\ \text{m}^3\right) = \boxed{1\times10^{-7}\ \text{J}}$$

From this kinetic energy, a velocity can be estimated assuming a density of 1 g/cm^3 for the displaced fluid:

$$K = \frac{1}{2}mv^2 = \frac{\rho V_{\text{hemi}}v^2}{2} \quad \rightarrow \quad v = \sqrt{\frac{2K}{\rho V_{\text{hemi}}}}$$
$$v = \sqrt{\frac{2\left(1\times10^{-7}\ \text{J}\right)}{\left(1\times10^{3}\ \text{kg/m}^3\right)\left(5.7\times10^{-12}\ \text{m}^3\right)}} = \boxed{6\ \text{m/s}} \qquad (11)$$

The maximum displacement Δx is the largest semi-axis of the hemi-ellipsoid, 190 μm. From this value and the velocity value in Eq. 11, an estimate of the time scale is obtained assuming constant acceleration:

$$t = \frac{2\Delta x}{v} = \frac{2\left(1.9\times10^{-4}\ \text{m}\right)}{\left(6\ \text{m/s}\right)} = \boxed{6\times10^{-5}\ \text{s}} = 0.06\ \text{ms} \qquad (12)$$

The average acceleration of the displaced fluid is estimated as:

$$a = \frac{v}{t} = \frac{\left(6\ \text{m/s}\right)}{\left(6\times10^{-5}\ \text{s}\right)} = \boxed{1\times10^{5}\ \text{m/s}^2} \approx 10000\ g \qquad (13)$$

The average acceleration of the fluid displaced by the expansion membrane is roughly the same as that of the spray pulse accelerating in the exit channel, which is consistent with the fact that the mass of the fluid displaced by the expansion membrane should be similar to that of the spray pulse (given their similar volumes and densities) and that similar forces are acting on both. The estimated membrane acceleration is also consistent with the observation that the vapor expansion occurs within one video frame (0.5 ms) which requires a minimum acceleration of:

$$\Delta x = \frac{1}{2} a_{\min} t^2 \quad \rightarrow \quad a_{\min} = \frac{2\Delta x}{t^2} = \frac{2\left(1.9\times10^{-4}\ \text{m}\right)}{\left(5\times10^{-4}\ \text{s}\right)^2} = \boxed{1.5\times10^{3}\ \text{m/s}^2} \tag{14}$$

Conversely, if one used the 2000-fps X-ray video alone to extract the membrane acceleration (e.g. by image tracking) rather than the energy arguments employed in this analysis, one would underestimate the acceleration (and the accompanying forces) by two orders of magnitude, because the time scale of the X-ray video frames (0.5 ms) is too coarse compared to the time scale of expansion (0.06 ms).

Energy Balance

Based on the estimated reactant droplet mass and the heat of reaction (0.8 J/mg, (*2*)), about 4×10^{-3} J is released in each explosion. The approximate energy balance is shown below, where E_{rxn} is the energy released in the explosion, K_{fluid} is the kinetic energy of the fluid displaced by the expansion membrane, K_{spray} is the kinetic energy of the spray pulse, Q_{spray} is the heat which raises the temperature of the spray pulse, and H_{vap} is the heat which boils the water content of the spray.

$$E_{\text{rxn}} = K_{\text{fluid}} + K_{\text{spray}} + Q_{\text{spray}} + H_{\text{vap}} \tag{15}$$

The kinetic energies are of order 10^{-7} J which is negligible compared to E_{rxn} of order 10^{-3} J. Therefore almost all of the energy goes into raising the temperature of the spray and boiling the water. Using the specific heat of water (~4000 J/kg/°C) to approximate that of the spray, the heat required to raise the temperature of the spray pulse from 20 °C to 100 °C is estimated:

$$Q_{\text{spray}} = m_{\text{spray}} c \Delta T = \left(5.5\times10^{-9}\ \text{kg}\right)\left(4000\ \text{J/kg°C}\right)\left(80\ \text{°C}\right) = \boxed{2\times10^{-3}\ \text{J}} \tag{16}$$

After heating the spray to 100 °C, about half of the energy released in the explosion (2×10^{-3} J) remains to boil the water. The water content of the reactant solution is about 55%, or 3 µg per droplet, and some additional water is produced in the explosion reaction. The enthalpy of evaporation for water is about 40 kJ/mol, or 2×10^{6} J/kg. The mass of water which is boiled by the remaining energy is estimated as:

$$\frac{\left(2\times10^{-3}\ \text{J}\right)}{\left(2\times10^{6}\ \text{J/kg}\right)} = 1\times10^{-9}\ \text{kg} = \boxed{1\ \mu\text{g}} \tag{17}$$

Thus, the heat given off in the explosion is sufficient to raise the spray temperature to 100 °C and boil about a third of the water content.

Kinematics of Inter-Chamber Valve Closure

The kinematics of valve closure will be modeled in three ways. First, only the effect of the dynamic pressure of fluid displaced by the expansion membrane will be considered. Second, the scenario of direct impingement of the expansion membrane on

the valve will be examined. Third, valve bending will be analyzed via energy considerations.

Dynamic pressure only. The fluid (hemolymph) displaced by the expansion membrane during the explosion will apply a dynamic pressure on the adjacent inter-chamber valve. Assuming constant fluid acceleration a_1 during the expansion, this pressure P_1 as a function of time (for the 0.06 ms duration of fluid acceleration) is estimated as the following, where ρ_1 is the density of the fluid, $v_1(t)$ is the fluid velocity, and $v(t)$ is the velocity of the valve relative to rest of the gland:

$$P_1(t) = \frac{\rho_1\left[v_1(t) - v(t)\right]^2}{2} = \frac{\rho_1\left[a_1 t - v(t)\right]^2}{2} \tag{18}$$

This pressure, acting on the area of the valve, accelerates the valve towards the closed position. A second dynamic pressure, due to the velocity of the valve relative to the fluid on the opposite side of the valve (reactant solution in the reservoir chamber) applies a force in the opposite direction. This pressure P_2 is estimated as the following, where ρ_2 is the density of the fluid:

$$P_2(t) = \frac{\rho_2 v(t)^2}{2} \tag{19}$$

The equation of motion of the valve relative to the gland, where τ_{valve} is the thickness of the valve, is approximated as the following:

$$\begin{aligned}
&\left[P_1(t) - P_2(t)\right] A_{valve} = m_{valve} a(t) \\
&m_{valve} = \rho_{valve} A_{valve} \tau_{valve} \quad \rightarrow \quad P_1(t) - P_2(t) = \rho_{valve} \tau_{valve} a(t) \\
&\frac{\rho_1\left[a_1 t - v(t)\right]^2 - \rho_2 v(t)^2}{2} = \rho_{valve} \tau_{valve} a(t) \\
&\rho_1 \approx \rho_2 \approx \rho_{valve} \quad \rightarrow \quad \left[a_1 t - v(t)\right]^2 - v(t)^2 = 2\tau_{valve} a(t) \\
&a(t) = \frac{1}{2\tau_{valve}}\left[\left(a_1 t - v(t)\right)^2 - v(t)^2\right]
\end{aligned} \tag{20}$$

Expressing Eq. 20 in terms of displacement and its derivatives gives a differential equation:

$$\frac{d^2x}{dt^2} = \frac{1}{2\tau_{valve}}\left[\left(a_1 t - \frac{dx}{dt}\right)^2 - \left(\frac{dx}{dt}\right)^2\right] \tag{21}$$

Taking values for the fluid average acceleration $a_1 = 1 \times 10^5$ m/s^2 as calculated in the previous section and estimating the average valve thickness $\tau_{valve} = 5$ μm, we obtain:

$$\frac{d^2x}{dt^2} = \frac{1}{\left(1\times10^{-5}\ \text{m}\right)}\left[\left(\left(1\times10^{5}\ \ \text{m/s}^2\right)t - \frac{dx}{dt}\right)^2 - \left(\frac{dx}{dt}\right)^2\right] \tag{22}$$

Numerical solution of Eq. 22 using the NDSolve operation in Mathematica (Wolfram Research, Champaign, IL, USA) for boundary conditions $x(t) = 0$ m and $x'(t) = 0$ m/s gives the displacement-time curve shown in Fig. S3A. At $t = 0.06$ ms, when the expansion membrane is expected to be maximally expanded, the displacement of the valve is predicted to be 80 μm, which Fig. S2C suggests is a reasonable estimate for the displacement needed to close the valve.

Direct impingement. With the expansion membrane directly impinging on the inter-chamber valve, the force applied to the valve equals the pressure inside the reaction chamber multiplied by the contact area. For purposes of calculation, contact over the entire valve area is assumed. The applied force causes the valve to accelerate towards the closed position. In doing so, the valve displaces fluid, creating a dynamic pressure in the opposite direction as in the previous scenario. The equation of motion is thus:

$$\begin{aligned}
&P_{\text{over}}A_{\text{valve}} - \frac{\rho_2 v(t)^2 A_{\text{valve}}}{2} = m_{\text{valve}}a(t) = \rho_{\text{valve}}A_{\text{valve}}\tau_{\text{valve}}a(t)\\
&P_{\text{over}} - \frac{\rho_2 v(t)^2}{2} = \rho_{\text{valve}}\tau_{\text{valve}}a(t)\\
&\rho_2 \approx \rho_{\text{valve}} \equiv \rho \quad \rightarrow \quad \frac{P_{\text{over}}}{\rho\tau_{\text{valve}}} - \frac{v(t)^2}{2\tau_{\text{valve}}} = a(t)\\
&a(t) = \frac{1}{2\tau_{\text{valve}}}\left[\frac{2P_{\text{over}}}{\rho} - v(t)^2\right]
\end{aligned} \tag{23}$$

Expressing Eq. 23 as a differential equation:

$$\frac{d^2x}{dt^2} = \frac{1}{2\tau_{\text{valve}}}\left[\frac{2P_{\text{over}}}{\rho} - \left(\frac{dx}{dt}\right)^2\right] \tag{24}$$

Using values of $\tau_{\text{valve}} = 5$ μm, $P_{\text{over}} = 20$ kPa, and $\rho = 1$ g/cm^3, we obtain:

$$\frac{d^2x}{dt^2} = \frac{1}{\left(1\times10^{-5}\ \text{m}\right)}\left[\left(4\times10^{1}\ \ \text{m}^2/\text{s}^2\right) - \left(\frac{dx}{dt}\right)^2\right] \tag{25}$$

Solving Eq. 25 numerically in Mathematica for boundary conditions $x(t) = 0$ m and $x'(t) = 0$ m/s gives the displacement-time curve shown in Fig. S3B, which indicates that direct impingement of the expansion membrane results in much more rapid displacement of the valve than dynamic pressure of the displaced fluid alone, with valve closure occurring in ~0.01 ms.

Valve bending. The previous kinematics treatments assume that the inter-chamber valve is free to displace at the connection with the reservoir chamber. If this connection is instead assumed to be fixed in space, then the valve will bend rather than displace. If we approximate the valve as a rectangular beam of dimensions ($b \times h \times l$) of 300 μm wide by 5 μm thick by 100 μm long, then the moment of inertia I is estimated as:

$$I = \frac{bh^3}{12} = \frac{\left(3\times10^{-4}\ \text{m}\right)\left(5\times10^{-6}\ \text{m}\right)^3}{12} = \boxed{3\times10^{-21}\ \text{m}^4} \tag{26}$$

The materials properties of the valve have not been measured experimentally; however, the valve stains purplish blue with toluidine blue and is digested by pancreatin, properties which are strongly suggestive of resilin (*31*) but not of typical nonsclerotized or sclerotized insect cuticles, and so for purposes of calculation we assume the valve material to be resilin with an elastic modulus of E = 1 MPa (*20*). We consider the loading scenario where a uniform pressure is imposed over the entire valve area, and the valve is considered closed when the valve tip has deflected 80 μm. Using beam bending theory (*32*) relating tip deflection δ_{tip} to load intensity q, the pressure required to close the valve is estimated as:

$$\begin{aligned}
&\delta_{\text{tip}} = \frac{ql^4}{8EI} \quad \rightarrow \quad q = \frac{8EI\delta_{\text{tip}}}{l^4} \\
&q = Pb \quad \rightarrow \quad P = \frac{q}{b} = \frac{8EI\delta_{\text{tip}}}{bl^4} \\
&P = \frac{8\left(1\times10^{6}\ \text{Pa}\right)\left(3\times10^{-21}\ \text{m}^4\right)\left(8\times10^{-5}\ \text{m}\right)}{\left(3\times10^{-4}\ \text{m}\right)\left(1\times10^{-4}\ \text{m}\right)^4} = \boxed{70\ \text{Pa}}
\end{aligned} \tag{27}$$

Thus the pressure needed to close the valve via bending is expected to be negligible compared to the pressure imposed by the expansion membrane, either directly or through fluid effects. The energy required for the deflection can be estimated from this pressure and the volume swept by the deflected valve, which is calculated as:

$$\delta(x) = \frac{qx^2}{24EI}\left(6l^2 - 4lx + x^2\right)$$

$$V = b \cdot \int_0^l \delta(x)\,dx = \frac{bq}{24EI}\left[6l^2\left(\frac{x^3}{3}\right) - 4l\left(\frac{x^4}{4}\right) + \frac{x^5}{5}\right]\Bigg|_0^l$$

$$V = \frac{bq}{24EI}\left(2l^5 - l^5 + \frac{l^5}{5}\right) = \frac{bq}{24EI}\left(\frac{6l^5}{5}\right) = \frac{bql^5}{20EI} \qquad (28)$$

$$q = Pb \quad \rightarrow \quad V = \frac{Pb^2l^5}{20EI}$$

$$V = \frac{\left(7\times10^{1}\ \text{Pa}\right)\left(3\times10^{-4}\ \text{m}\right)^2\left(1\times10^{-4}\right)^5}{20\left(1\times10^{6}\ \text{Pa}\right)\left(3\times10^{-21}\ \text{m}^4\right)} = \boxed{1\times10^{-12}\ \text{m}^3}$$

The work (strain energy) required to bend the valve is thus estimated as:

$$W = PV = \left(7\times10^{1}\ \text{Pa}\right)\left(1\times10^{-12}\ \text{m}^3\right) = \boxed{6\times10^{-11}\ \text{J}} \qquad (29)$$

This value is several orders of magnitude lower than the kinetic energy of the fluid displaced by the expansion membrane (1×10^{-7} J), and therefore the energy of bending can be neglected and it is only necessary to consider the dynamic pressure of the fluid accelerated by the valve. Thus, the valve bending scenario reduces to the displacement scenarios previously considered, in which valve motion is resisted principally by the fluid behind the valve.

Author Contributions

W.M. collected and identified live beetles. E.M.A. and W.M. maintained live beetles for experiments and handled beetles for synchrotron experiments. E.M.A., W.M., and W.-K.L. performed synchrotron experiments. E.M.A. and W.-K.L. processed data from synchrotron experiments. E.M.A. analyzed data from synchrotron experiments. W.M. and E.M.A. performed dissections. W.M. identified the expansion membrane and provided optical micrographs. E.M.A. provided electron micrographs. E.M.A, W.M., and W.-K.L. interpreted results. E.M.A. prepared figures, tables, and movies and wrote draft manuscript. C.O. initiated and supervised all aspects of the project. All authors revised manuscript for submission.

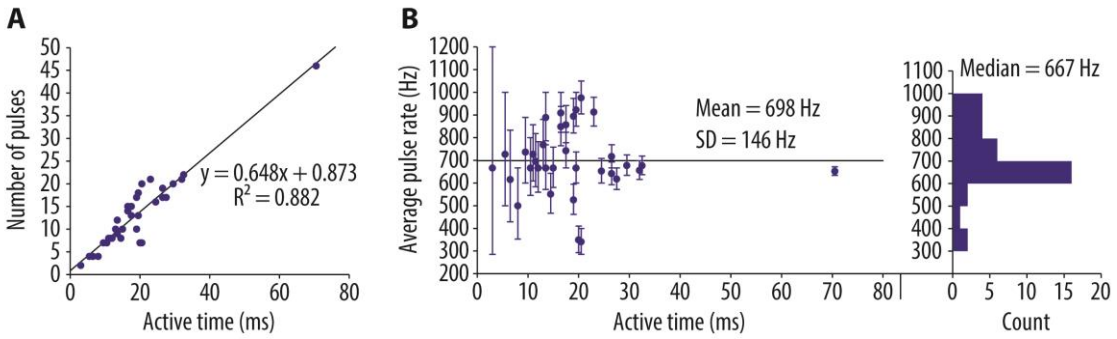

Fig. S1.

Quantification of spray pulsation rates. (**A**) Plot of number of pulses vs. active time for periods of gland activity recorded with 2000-fps synchrotron X-ray phase-contrast imaging. Nominal uncertainties for each data point are ±1 pulse and ±0.5 ms (1 frame). (**B**) Plot of average pulsation rate versus active time for periods of gland activity recorded at 2000 fps, with histogram representation at right. Error bars reflect range of possible values assuming nominal uncertainties for number of pulses and active time.

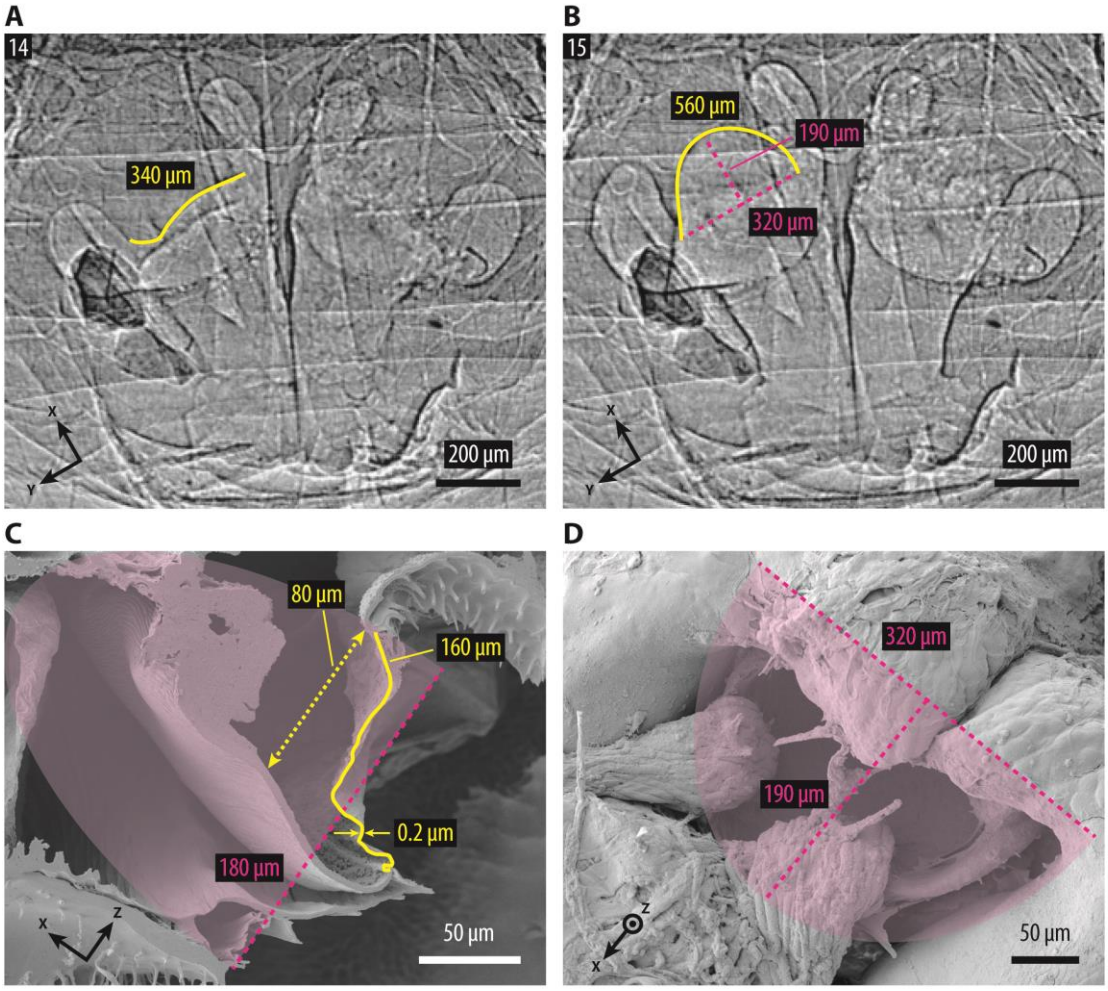

Fig. S2

Expansion membrane displacement and included volume. (**A**) Determination of coronal cross-sectional length of relaxed expansion membrane (yellow trace), as estimated from X-ray video (Fig. 2A frame 14). (**B**) Coronal cross-sectional length of stretched expansion membrane (yellow trace) and estimated hemi-ellipsoid (semi-)axes (magenta dashed lines), based on Fig. 2A frame 15. (**C**) Sagittal cross-sectional length of relaxed expansion membrane (solid yellow trace), estimated minimum valve displacement needed for valve closure (yellow dashed line), and estimated ellipsoid semi-axis (magenta dashed line) as measured from SEM (Fig. 1E). Superimposed magenta hemi-ellipse represents sagittal cross-section of volume included by stretched expansion membrane. (**D**) SEM image (Fig. 1D) with superimposed hemi-ellipse representing coronal cross-section of volume included by stretched expansion membrane. Orthogonal *xyz* axes coincide with hemi-ellipsoid axes.

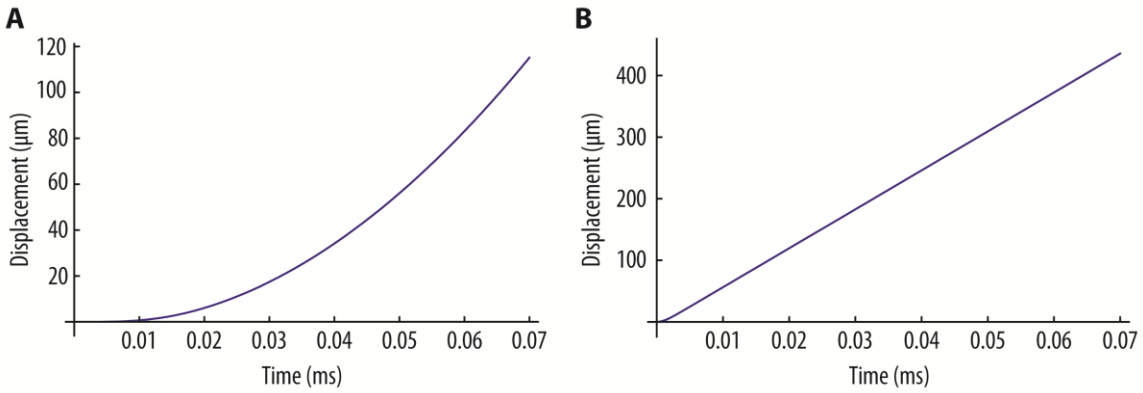

Fig. S3

Predicted displacement versus time for inter-chamber valve for scenarios of (**A**) dynamic pressure of fluid displaced by expansion membrane and (**B**) direct impingement of expansion membrane. Maximum expansion occurs at t = 0.06 ms in A. Displacements larger than ~200 µm are not meaningful.

Table S1.

Durations of sprays recorded by synchrotron X-ray phase-contrast imaging: (top) details and (bottom) summary. Uncertainties in duration are nominal. Beetles and sprays are listed in the order in which they were recorded.

Imaging rate (fps)	Beetle	Sex	Spray #	# of glands active	Duration (frames)	Duration (ms)
30	1	female	1	2	2 ± 1	67 ± 33
			2	2	1 ± 1	33 ± 33
250	2	female	1	1	15 ± 1	60 ± 4
			2	1	27 ± 1	108 ± 4
			3	1	86 ± 1	344 ± 4
	3	male	1	2	7 ± 1	28 ± 4
			2	2	9 ± 1	36 ± 4
			3	2	8 ± 1	32 ± 4
	4	male	1	2	6 ± 1	24 ± 4
1000	5	male	1	2	23 ± 1	23 ± 1
2000	6	female	1	2	141 ± 1	70.5 ± 0.5
	7	male	1	2	38 ± 1	19.0 ± 0.5
	8	male	1	2	35 ± 1	17.5 ± 0.5
			2	2	46 ± 1	23.0 ± 0.5
			3	2	42 ± 1	21.0 ± 0.5
	9	male	1	2	35 ± 1	17.5 ± 0.5
	10	male	1	2	41 ± 1	20.5 ± 0.5
	11	male	1	2	49 ± 1	24.5 ± 0.5
			2	2	34 ± 1	17.0 ± 0.5
			3	1	13 ± 1	6.5 ± 0.5
			4	1	19 ± 1	9.5 ± 0.5
			5	2	34 ± 1	17.0 ± 0.5
			6	2	24 ± 1	12.0 ± 0.5
	12	male	1	2	53 ± 1	26.5 ± 0.5
			2	2	64 ± 1	32.0 ± 0.5
			3	2	66 ± 1	33.0 ± 0.5
			4	2	19 ± 1	9.5 ± 0.5
	13	male	1	2	33 ± 1	16.5 ± 0.5
	14	male	1	1	10 ± 1	5.0 ± 0.5
			2	2	143 ± 1	71.5 ± 0.5

Median duration (ms)	Min. value (ms)	Max. value (ms)
23.5	5.0 ± 0.5	344 ± 4

Table S2.

Average pulsation rates calculated for periods of gland activity recorded with 2000-fps synchrotron X-ray phase-contrast imaging: (top) details and (bottom) summary. Uncertainties in pulsation rate represent range of possible values calculated assuming nominal uncertainties of ±1 pulse and ±0.5 ms (1 frame) for the number of pulses and the active time, respectively. Beetles, sprays, and periods of gland activity are listed in the order in which they were recorded.

Beetle	Sex	Spray #	Gland	Active time (ms)	# of pulses	Avg. pulsation rate (Hz)	Uncertainty (Hz)
6	female	1	right	70.5 ± 0.5	46 ± 1	653	+19 / −19
			left	26.5 ± 0.5	19 ± 1	717	+52 / −50
			left	13.5 ± 0.5	9 ± 1	667	+103 / −95
7	male	1	right	19.0 ± 0.5	10 ± 1	526	+68 / −65
			left	14.5 ± 0.5	8 ± 1	552	+91 / −85
8	male	1	right	17.5 ± 0.5	15 ± 1	857	+84 / −79
			left	16.5 ± 0.5	14 ± 1	848	+89 / −84
		2	left	23.0 ± 0.5	21 ± 1	913	+65 / −62
			right	20.5 ± 0.5	20 ± 1	976	+74 / −71
		3	left	19.5 ± 0.5	18 ± 1	923	+77 / −73
			right	19.0 ± 0.5	17 ± 1	895	+78 / −74
9	male	1	left	17.5 ± 0.5	13 ± 1	743	+81 / −76
			right	11.0 ± 0.5	8 ± 1	727	+130 / −119
10	male	1	left	20.5 ± 0.5	7 ± 1	341	+59 / −56
			right	20.0 ± 0.5	7 ± 1	350	+60 / −57
11	male	1	right	24.5 ± 0.5	16 ± 1	653	+55 / −53
			left	19.5 ± 0.5	13 ± 1	667	+70 / −67
		2	right	11.5 ± 0.5	8 ± 1	696	+123 / −112
			left	3.0 ± 0.5	2 ± 1	667	+533 / −381
		3	right	6.5 ± 0.5	4 ± 1	615	+218 / −187
		4	right	9.5 ± 0.5	7 ± 1	737	+152 / −137
		5	right	13.0 ± 0.5	10 ± 1	769	+111 / −103
			left	15.0 ± 0.5	10 ± 1	667	+92 / −86
		6	right	12.0 ± 0.5	8 ± 1	667	+116 / −107
			left	10.5 ± 0.5	7 ± 1	667	+133 / −121
12	male	1	left	26.5 ± 0.5	17 ± 1	642	+51 / −49
			right	24.5 ± 0.5	16 ± 1	653	+55 / −53
		2	left	32.0 ± 0.5	21 ± 1	656	+42 / −41
			right	29.5 ± 0.5	20 ± 1	678	+46 / −45
		3	left	32.5 ± 0.5	22 ± 1	677	+42 / −41
			right	27.5 ± 0.5	17 ± 1	618	+48 / −47
		4	left	5.5 ± 0.5	4 ± 1	727	+273 / −227
			right	8.0 ± 0.5	4 ± 1	500	+167 / −147

13	male	1	left	16.5 ± 0.5	15 ± 1	909	+91 / −86
			right	13.5 ± 0.5	12 ± 1	889	+111 / −103

Mean (Hz)	Std. dev. (Hz)	Std. error (Hz)	Median (Hz)	Min. value (Hz)	Max. value (Hz)
698	146	25	667	341	976

Movie S1

X-ray video of a spray by a male *B. elongatulus* (beetle 7 in Tables S1 and S2; see also Fig. 2A) recorded at 2000 fps, slowed down 80× (25-fps playback).

Movie S2

X-ray video of a spray by a male *B. elongatulus* (beetle 10 in Tables S1 and S2; see also Fig. 2B) recorded at 2000 fps, slowed down 80× (25-fps playback).

Movie S3

X-ray video of a spray by a female *B. elongatulus* (beetle 6 in Tables S1 and S2) recorded at 2000 fps, slowed down 80× (25-fps playback).